

See discussions, stats, and author profiles for this publication at: <https://www.researchgate.net/publication/231238504>

Ca Doping of Nanosize Ce–Zr and Ce–Tb Solid Solutions: Structural and Electronic Effects

ARTICLE · JULY 2005

DOI: 10.1021/cm050265i

CITATIONS

33

READS

42

6 AUTHORS, INCLUDING:



Marcos Fernández-García

Spanish National Research Council

260 PUBLICATIONS **8,623** CITATIONS

SEE PROFILE



C. Belver

Universidad Autónoma de Madrid

57 PUBLICATIONS **1,581** CITATIONS

SEE PROFILE



Jonathan Hanson

Brookhaven National Laboratory

174 PUBLICATIONS **6,787** CITATIONS

SEE PROFILE

Ca Doping of Nanosize Ce–Zr and Ce–Tb Solid Solutions: Structural and Electronic Effects

Marcos Fernández-García,^{*,†} Xianqin Wang,[‡] Carolina Belver,[†] Ana Iglesias-Juez,[†] Jonathan C. Hanson,[‡] and José A. Rodríguez^{*,‡}

*Instituto de Catálisis y Petroleoquímica, CSIC, Campus Cantoblanco, 28049 Madrid, Spain, and
Department of Chemistry, Brookhaven National Laboratory, Upton, New York 11973*

Received February 4, 2005. Revised Manuscript Received June 7, 2005

Ceria-based ternary oxides are novel materials with potential use in many areas of chemistry, physics, and materials science. Synchrotron-based time-resolved X-ray diffraction (TR-XRD), X-ray absorption near-edge spectroscopy (XANES), Raman and infrared spectroscopies (RS and IR), and density-functional (DF) calculations were used to study the structural and electronic properties of Ce–M–Ca (M = Zr, Tb) oxide nanoparticles. The nanoparticles were synthesized following novel microemulsion and citrate methods and had sizes in the range of 3–6 nm. The atoms in these nanoparticles adopted a Fluorite-type structure and exhibited cell parameters with deviations with respect to the values predicted by Vegard's rule for ideal solid solutions. The simultaneous presence of Zr/Tb and Ca creates strain in the Fluorite-type lattice which correlates with the presence and number of oxygen vacancies through the Ce–M–Ca samples. The oxygen vacancy and cation distributions of the nanoparticles are strongly affected by the preparation method. The XANES/density-functional theory study indicates that Ce–M–Ca solid solutions display distinctive electronic properties. In the Ce–Zr–Ca system, the Zr(4d) splitting into t_{2g} and e_g orbitals is affected by the presence of Ca, leaving the Ce orbitals mostly unaffected. This is a consequence of the local environment of the Zr cations, which is modified from a monoclinic-like to a tetragonal (t'') symmetry as the Ca content rises. In Ce–Tb–Ca solid solutions, there is a progressive stabilization of the fully oxidized Tb state (Tb^{4+}) as the Ca content increases, mainly to minimize the strain of the structure. In both systems, $Ca^{2+} \leftrightarrow O^{2-} \leftrightarrow M^{n+}$ interactions play a major role in the structural and electronic properties and are critical to interpret the thermal behavior of the materials.

I. Introduction

Ceria (CeO_2) is an oxide with important implications in areas of catalysis, electrochemistry, photochemistry, and materials science.^{1–3} Novel applications of Ce-based oxides use binary oxide solid solutions whose performance primarily depends on the particle size, structural characteristics, and the chemical nonstoichiometry.^{3–5} Among these Ce-based solid solutions, Ce–Zr^{5–8} and Ce–Tb^{5,9–11} have lead to

materials with enhanced oxygen handling properties and thermal stability. The two types of properties are of importance in combustion/oxidation reactions taking place in automobile converters and solid-oxide fuel cells,^{3–6} while the first is additionally utilized in the separation of air^{12,13} and cryogenic refrigeration.¹⁴ Optimum properties for the applications mentioned above are typically reached in both Ce–Zr and Ce–Tb cases with a stoichiometry approaching a 1:1 Ce/M (M = Zr, Tb) atomic ratio.^{3–11} On the other hand, nanoparticle configurations are interesting from a practical viewpoint as most of the applications mentioned are surface-sensitive, and a high surface-to-volume ratio in addition to improved redox properties, related to oxygen vacancy generation, can be reached by using nanosize materials.^{3,5,6,8,10,11,15,16} The employment of preparation methods leading to homodisperse materials can produce, in

* Corresponding authors. E-mail: mfg@icp.csic.es (M.F.-G.); rodriguez@bnl.gov (J.A.R.).

† CSIC.

‡ Brookhaven National Laboratory.

- (1) Henrich, V. E.; Cox, P. A. *The Surface Science of Metal Oxides*; Cambridge University Press: Cambridge, U.K., 1994.
- (2) (a) Wells, A. F. *Structural Inorganic Chemistry*, 6th ed.; Oxford: New York, 1987. (b) Shelef, M.; Graham, C. W. *Catal. Rev. Sci. Eng.* **1994**, *36*, 433. (c) *Application of Solid Electrolytes*; Takahashi, T., Kozawa, A., Eds.; JEC Press: Cleveland, OH, 1980. (d) Inaba, H.; Tagawa, H. *Solid State Ionics* **1996**, *83*, 1.
- (3) *Catalysis by Ceria and Related Materials*; Trovarelli, A., Ed.; World Scientific: London, 2002.
- (4) Kofsta, P. *Non-stoichiometry, Diffusion and Electrical Conductivity of Binary Mixed Oxides*; Wiley: New York, 1972.
- (5) Fernández-García, M.; Martínez-Arias, A.; Hanson, J. C.; Rodríguez, J. A. *Chem. Rev.* **2004**, *104*, 4063.
- (6) (a) Kaspar, J.; Fornasiero, P.; Graziani, M. *Catal. Today* **1999**, *50*, 205. (b) Kaspar, J.; Fornasiero, P. *J. Solid State Chem.* **2003**, *171*, 19.
- (7) Si, R.; Zhang, Y.-W.; Li, S.-J.; Yan, C.-H. *J. Phys. Chem. B* **2004**, *108*, 12481.
- (8) Rodríguez, J. A.; Hanson, J. C.; Kim, J.-Y.; Liu, G.; Iglesias-Juez, A.; Fernández-García, M. *J. Phys. Chem. B* **2003**, *107*, 3535.
- (9) Zamar, F.; Trovarelli, A.; de Leitenbrug, C.; Dolcetti, G. *Stud. Surf. Sci. Catal.* **1996**, *101*, 1283.

- (10) (a) Bernal, S.; Blanco, G.; Cauqui, M. A.; Corchado, M. P.; Pintado, J. M.; Rodríguez-Izquierdo, J. M. *Chem. Commun.* **1997**, 1545. (b) Bernal, S.; Blanco, G.; Delgado, J. J.; Pintado, J. M.; Larese, C.; Rodríguez-Izquierdo, J. M. *Catal. Today* **1999**, *53*, 607. (c) Bernal, S.; Blanco, G.; Delgado, J. J.; Pintado, J. M.; Rodríguez-Izquierdo, J. M. *J. Alloys Compd.* **2002**, *344*, 347.
- (11) (a) Hungria, A. B.; Martínez-Arias, A.; Fernández-García, M.; Iglesias-Juez, A.; Guerrero-Ruiz, A.; Calvino, J. J.; Conesa, J. C.; Soria, J. *Chem. Mater.* **2003**, *15*, 4309. (b) Wang, X.; Hanson, J. C.; Liu, G.; Rodríguez, J. A.; Iglesias-Juez, A.; Fernández-García, M. *J. Chem. Phys.* **2004**, *121*, 5434.
- (12) Malhaupt, J. T.; Waldwik, K. U.S. Patent 3,980,765, 1976.
- (13) Jones, J. A.; Blue, G. D. *J. Spacecraft* **1988**, *25*, 202.
- (14) Shuk, P.; Greeblatt, M.; Croft, M. *Chem. Mater.* **1999**, *11*, 473.

contrast with solid state techniques, nanosize materials with high structural and chemical homogeneity, which, apparently, display improved performance, particularly thermal stability, with respect to nonhomogeneous materials.^{3,5,6}

Ceria-based ternary oxide solid solutions^{17–24} have been less investigated than binary compounds,^{1–11} but their technological importance is expected to be high soon as they constitute a natural way to improve the properties of nowadays standard binary oxide solid solutions. In the most simple approximation, one can assume that the structural and electronic properties of a mixed-metal oxide are an interpolation of the properties of the single oxides, that is, there is an absence of metal ↔ oxygen ↔ metal interactions.^{25,26} In this respect, Ce-based binary solid solutions mostly behave as ideal ones; they obey the Vegard's rule^{3,5–11} and their electronic properties change rather smoothly with respect to ceria.^{5,6,8,11} A special case may concern Ce–Tb solid solutions as a decreasing quantity of the lower oxidation state (Tb³⁺) has been noticed as the Tb content of the material grows.^{10,11} The more or less “ideal behavior” may not be, however, followed by Ce-based ternary oxides²⁴ as a consequence of structural and electronic perturbations of metal ↔ oxygen ↔ metal and higher-order interactions. It is important to identify these structural and electronic perturbations because they can determine chemical reactivity of Ce-based materials.^{1–5}

In this article we focus on the analysis of Ca-containing Ce–Zr and Ce–Tb ternary solid solutions. Ca has been shown to maximize the oxygen storage of Ce-based materials,¹⁷ and Ce–Ca materials have practical application on the destruction of SO₂.²⁷ Also, Ce–Zr–Ca oxides are formed by contact between Ceria-based and Ca-doped Zirconia components of fuel cells under operation.¹⁸ For such practical reasons as well as for academic reasons^{1–5,28} it is important

to gain further insight into the behavior of Ca-doped Ce-based ternary oxide solid solutions. In this article we investigate the structural and electronic properties of Ce–M–Ca oxide nanoparticles using X-ray absorption near-edge spectroscopy (XANES), Raman and infrared spectroscopies (RS/IR), time-resolved X-ray diffraction (TR-XRD), and first-principles density-functional (DF) calculations. Our results clearly show that Ca addition to binary Ce–Zr and Ce–Tb solid solutions gives distinctive properties not seen from parent (single or binary) oxides. A second objective of the study is to compare the performance of two preparation methods specifically devised to yield nanosize materials. In our case, this objective has been particularly focused on the analysis of the thermal stability of the solid solutions.

II. Experimental and Theoretical Methods

II.1. Preparation of the Ce–Zr–Ca and Ce–Tb–Ca Oxides.

Oxide nanoparticles containing Ce, M (Zr and Tb), and Ca were prepared using an adaptation of the microemulsion method used previously for the synthesis of Ce–Zr and Ce–Tb binary solid solutions.^{8,11,28} The microemulsion method is based on the preparation of water in organic microemulsions, constituted by small water droplets in which metal precursors can be dissolved for obtaining final metal oxide nanoparticles. For this purpose, a microemulsion formed by a base-containing aqueous solution is added to other microemulsions containing the (Ce, Zr, Ca) nitrate metal salts (changing the metal ratios but fixing the metal concentration), and the addition causes the hydrolysis of the metals and the corresponding hydroxide precipitation. The final calcination of the precipitate at 500 °C yields the desired mixed oxide. An additional citrate method was used for the synthesis of Ce–Zr–Ca samples. This latter method essentially consists of a sol–gel process using metal–citrate precursors. These precursors are aqueous solutions of nitrate metal salts and citric acid of known concentrations. When the mole ratios of the metals, the pH, and the temperature are controlled, it is possible to obtain a black viscous precursor, which drying and subsequent calcination at 600 °C produces the formation of the wanted mixed oxide. As a result, a total of three series of samples, called CZAm, CZAc, and CTAm (where C, Z, T, and A stand for Ce, Zr, Tb and Ca, and c/m indicates the series prepared by the citrated/microemulsion method), were synthesized. For each series, one of the samples contained equal amounts of the three cations, Ce_{0.33}Zr_{0.33}Ca_{0.33}O₂ (CZA111/CZA111c in our notation) and Ce_{0.33}Tb_{0.33}Ca_{0.33}O₂ (CTA111). We also examined samples that had equal amounts of Ce and Zr or Tb and growing quantities of Ca, Ce_{0.45}M_{0.45}Ca_{0.1}O₂, and Ce_{0.4}M_{0.4}Ca_{0.2}O₂, with M = Zr, Tb (CZA992/CZA992c/CTA992 and CZA442/CZA442c/CTA442 in our notation). References for Ce–Zr, Ce–Tb, and Ce–Ca systems having equal amounts (or a 2:1 ratio) of the two cations were labeled as CZ11, CT11, and CA21, respectively. In these ternary systems, there are oxygen vacancies present (i.e., oxygen/metal ratio < 2), but for simplicity we will label and refer to them as Ce_{1–x–y}M_xCa_yO₂ or by the CMZxxx(c) notation.

II.2. TR-XRD Experiments. The TR-XRD data were collected at beamlines X7B ($\lambda = 0.9220 \pm 0.0005$ Å) and X17B1 ($\lambda = 0.1655 \pm 0.0005$ Å) of the National Synchrotron Light Source (NSLS) in Brookhaven National Laboratory (BNL). An identical setup system was employed in both beamlines.^{8,24,28} The wavelength calibration was determined with the FIT2D code based on the diffraction pattern for LaB₆.^{8,28,29} In the TR-XRD experiments dealing with the thermal stability and sintering of the Ce_{1–x–y}Zr_xTb_yO₂ nanoparticles, the sample was kept in a sapphire capillary and heated

- (15) Tsunekawa, S.; Ishikawa, K.; Li, Z. Q.; Kawazoe, Y.; Kasuya, A. *Phys. Rev. Lett.* **2000**, *85*, 3340.
- (16) Spanier, J. E.; Robinson, R. D.; Zhang, F.; Chan, S.-W.; Herman, I. P.; *Phys. Rev. B* **2001**, *64*, 245407.
- (17) Zhang, Y.; Anderson, S.; Muhammed, M. *Appl. Catal. B* **1995**, *6*, 325.
- (18) Nigara, Y.; Watanabe, K.; Kawamura, K.; Mizusaki, J.; Kawada, T. *J. Am. Ceram. Soc.* **1997**, *144*, 1050.
- (19) Terribile, D.; Trovarelli, A.; de Leitenburg, C.; Primavera, A.; Dolcetti, G. *Catal. Today* **1999**, *47*, 133.
- (20) Karula, C. K.; Haack, L. P.; Chun, W.; Jen, H. W.; Graham, G. W. *J. Phys. Chem. B* **1999**, *103*, 3634.
- (21) Ikryannikova, L. N.; Aksekov, A. A.; Markaryan, G. L.; Muravéva, G. P.; Kostyuk, B. G.; Kharlanov, A. N.; Lunina, E. V. *Appl. Catal. A* **2001**, *210*, 225.
- (22) Kimpton, J.; Rendle, T. H.; Dennen, J. *J. Solid State Chem.* **2002**, *199*, 89.
- (23) Fernández-García, M.; Martínez-Arias, A.; Guerrero-Ruiz, A.; Conesa, J. C.; Soria, J. *J. Catal.* **2002**, *211*, 326.
- (24) Wang, X.; Hanson, J. C.; Rodríguez, J. A.; Belver, C.; Fernández-García, M. *J. Chem. Phys.* **2005**, *122*, No. 154711.
- (25) Harrison, W. A. *Electronic Structure and the Properties of Solids*; Dover: New York, 1980.
- (26) (a) Weller, M. T. *Inorganic Materials Chemistry*; Oxford, New York, 1994. (b) West, A. R. *Solid State Chemistry and its Applications*; Wiley: New York, 1997.
- (27) de Carolis, S.; Pascual, J. L.; Pettersson, L. G. M.; Baudin, M.; Wojcik, M.; Hermansson, K.; Palmqvist, A. E. C.; Muhammed, M. *J. Phys. Chem. B* **1999**, *103*, 7627.
- (28) (a) Iglesias-Juez, A.; Hungria, A. B.; Gálvez, O.; Martínez-Arias, A.; Fernández-García, M.; Conesa, J. C.; Soria, J.; *Stud. Surf. Sci. Catal.* **2001**, *138*, 347. (b) Rodríguez, J. A.; Wang, X.; Hanson, J. C.; Liu, G.; Iglesias-Juez, A.; Fernández-García, M. *J. Chem. Phys.* **2003**, *119*, 5659.

using a small resistance heater placed around the capillary.²⁹ A chromel–alumel thermocouple was used to measure the temperature of the sample. Two-dimensional powder patterns were collected with a Mar345 image plate detector, and the powder rings were integrated using the FIT2D code.³⁰ From the XRD data, accurate lattice constants were determined by a Rietveld analysis using the GSAS (general structure analysis system) program.³¹ To calculate the strain in the lattice of the $\text{Ce}_{1-x}\text{Zr}_x\text{Tb}_y\text{O}_2$ samples, we used the commercial Reflex package³² provided by Accelrys. The instrument parameters were derived from the fit of a Si reference pattern to the Thompson–Cox–Hastings profile coefficients^{32b} and Berar–Baldinozzi asymmetry correction.^{32c} Then, the sample size^{32d} and strain ($\Delta a/a$, a = cell constant)^{32e} were determined from the peak broadening in the nanoparticles. From the variation of the peak width with 2θ in powder diffraction, one can obtain a strain parameter^{32e} that is a measure of the lattice stress existing in the oxide because of crystal imperfections:⁵ oxygen vacancies, other point defects, line defects, and plane defects.

II.3. XANES Experiments. The K-edge spectrum of Ca and the L_{III} -edge spectra of Ce, Zr, and Tb were collected at the NSLS on beam line X19A in the “fluorescence-yield mode” using a boomerang-type flat crystal monochromator and a special cell with a modified Stern–Heald–Lytle detector.^{8,11b} All the XANES spectra were taken at room temperature using a constant scan step of 0.5 eV through the edge region, and the energy resolution was close to 0.5–1.0 eV.

II.4. RS and IR Spectroscopy Experiments. RS spectra were obtained at room temperature with a Renishaw Dispersive system 1000, equipped with a cooled TCD and holographic Notch filter. The samples were excited with the 633 nm He:Ne laser line, and the spectra consisted of 50 accumulations with a total of 10–15 min of acquisition time, using a typical running power of 2–10 mW. Care was taken in minimizing heating of the samples; peak positions were found to be constant within 2–3 cm^{-1} .

Diffuse reflectance infrared spectra (DRIFTS) were taken in Bruker Equinox 55 Fourier transform infrared spectrometer fitted with a mercury cadmium telluride detector. The spectra consisted of 400 accumulations with a total of 5 min of acquisition time, using a 4- cm^{-1} resolution.

II.5. Thermogravimetric Measurements. Analysis of carbonate-like phases present on the materials was performed by using a thermogravimetric-mass spectrometer (TG-MS) system from Perkin-Elmer TG-7. Samples were treated in dry air up to the calcination temperatures and cooled in nitrogen. After the pretreatment they were subjected to a heating ramp of 20 $^{\circ}\text{C min}^{-1}$ from 25 to 925 $^{\circ}\text{C}$ under a 20% O_2/N_2 . The evolving gaseous products were detected by mass spectrometry; only $\text{CO}_2(\text{g})$ ($m/z = 44$) was observed in the experiments as a carbon-containing molecule.

II.6. Theoretical Methods. The first-principles DF calculations reported in section III were performed using the CASTEP (Cam-

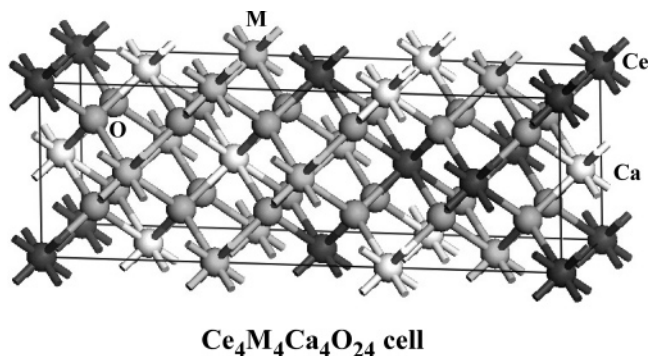


Figure 1. Unit cell used to study the properties of bulk Ce–M–Ca (1:1:1) solid solution. The unit cell contains 4 atoms of Ce, 4 atoms of M, 4 atoms of Ca, and 24 atoms of O. The positions of the metal cations were exchanged in the unit cell to reflect a random solid solution (see text). In the figure is shown a possible configuration for the ternary oxide.

bridge Serial Total Energy Package) suite of programs.²⁶ CASTEP has an excellent track record in accurate prediction of geometry and energy for oxide systems.^{8,11b,28b,33a,34} In this code, the wave functions of valence electrons are expanded in a plane wave basis set with k vectors within a specified energy cutoff E_{cut} . Tightly bound core electrons are represented by nonlocal ultrasoft pseudopotentials.³⁵ Brillouin Zone integration is approximated by a sum over special k points chosen using the Monkhorst–Pack scheme.³⁶ In all the calculations, the kinetic energy cutoff E_{cut} (400 eV) and the density of the Monkhorst–Pack k -point mesh were chosen high enough to ensure convergence of the computed structures and energies. The exchange-correlation contribution to the total electronic energy was treated in a generalized-gradient corrected form of the local density approximation: Perdew–Burke–Ernzerhoff functional.³⁷

To investigate the properties of the bulk Ce–M–Ca oxide, we employed the cell shown in Figure 1, which contained 24 O atoms plus 4 atoms of Ce, M ($\text{M} = \text{Zr}, \text{Tb}$), and Ca (12 metal atoms in total). In a first approximation, the atoms of M and Ca were set in the pattern shown in Figure 1. Then, possible permutations for the four M and four Ca atoms were considered, and the properties of materials were determined by taking an average over all these permutations.³⁸ For each one of these permutations, we relaxed the crystal geometry, before obtaining average values of lattice constants, metal–oxygen distances, charges, and so forth. The structural parameters of bulk CeO_2 and the Ce–M–Ca systems in its different configurations were determined using the Broyden–Fletcher–Goldfarb–Shanno (BFGS) minimization technique, with the following thresholds for the converged structures: energy change per atom less than 5×10^{-6} eV, residual force less than 0.02 eV/Å, the displacement of atoms during the geometry optimization less than 0.001 Å, and the root mean square of the stress tensor less than 0.1 GPa.

For each optimized structure, the partial charges on the atoms were estimated by projecting the occupied one-electron eigenstates

- (29) (a) Norby P.; Hanson, J. *Catal. Today* **1998**, 39, 301 and references therein. (b) Chupas, P. J.; Ciruolo, M. F.; Hanson, J. C.; Grey, C. P. *J. Am. Chem. Soc.* **2001**, 123, 1694.
- (30) Hammersely, A. P.; Svensson, S. O.; Thompson, A. *Nucl. Instrum. Methods Phys. Res.* **1994**, 346, 321.
- (31) (a) Larson, A. C.; von Dreele, R. B. *GSAS General Structure Analysis System*; Report LAUR 86-748; Los Alamos National Laboratory: Los Alamos, NM, 1995. (b) Reitveld, A. M. *J. Appl. Crystallogr.* **1969**, 2, 65. Values of a obtained taking into consideration asymmetry effects are a little bit different (0.01–0.02 Å) from those obtained ignoring asymmetry.^{8,28b} Independently of this, variations of the same order in the lattice dimension can be expected depending on the exact experimental procedure used for the preparation of the nanoparticles.
- (32) (a) Reflex package provided by Accelrys. (b) Thompson, P.; Cox, D. E.; Hastings, J. B. *J. Appl. Crystallogr.* **1987**, 20, 79. (c) Baldinozzi, J.; Berar, J. F. *J. Appl. Crystallogr.* **1993**, 26, 128. (d) Scherrer, P. *Gott. Nachr.* **1918**, 2, 98. (e) Young, R. A. *The Rietveld Method*; Oxford Press: Oxford, 1993 (IUCR Mono. Cryst. 5).

- (33) (a) Milman, V.; Winkler, B.; White, J. A.; Pickard, C. J.; Payne, M. C.; Akhmatkaya, E. V.; Nobes, R. H. *Int. J. Quantum Chem.* **2000**, 77, 895. (b) Payne, M. C.; Allan, D. C.; Arias, T. A.; Johannopoulos, J. D. *Rev. Mod. Phys.* **1992**, 64, 1045.
- (34) (a) Rodriguez, J. A. *Theor. Chem. Acc.* **2002**, 107, 117. (b) Dawson, I.; Bristowe, P. D.; Lee, M. H.; Payne, M. C.; Segall, M. D.; White, J. M. *Phys. Rev. B* **1996**, 54, 13727. (c) Lindan, P. J. D.; Harrison, N. M.; Holender, J. M.; Gillan, M. J. *Chem. Phys. Lett.* **1996**, 261, 246.
- (35) Vanderbilt, D. *Phys. Rev. B* **1990**, 41, 7892.
- (36) Monkhorst, H. J.; Pack, J. D. *Phys. Rev. B* **1976**, 13, 5188.
- (37) Perdew, J. P.; Burke, K.; Ernzerhof, M. *Phys. Rev. Lett.* **1996**, 77, 3865.
- (38) Rodriguez, J. A.; Etxebarria, A.; González, L.; Maiti, A. *J. Chem. Phys.* **2002**, 117, 2699.

onto a localized basis set (which included pseudo-orbitals representing the valence levels of O, Ce, Zr, Tb, and Ca) with a subsequent Mulliken population analysis.³⁹ Any charge partition scheme has approximations,⁴⁰ but the Mulliken analysis has been shown frequently to be useful for studying qualitative trends in charge distribution.^{8,11,28}

III. Results and Discussion

III.1. Analysis of Carbonate Phases. As it is well-known, Ca-containing samples may contain a small amount of carbonate phases even if they are not detected as a separate phase by diffraction techniques.^{23,28} A TG-MS analysis in dry air showed evolution of CO₂ to the gas phase at temperatures above 700 °C, indicating the presence of carbonate phases in our samples. IR allows the nature of such phases to be discerned, giving evidence of the presence of Ca carbonates and, to a much less extent, of other (mainly Ce) carbonates (Figure 2). The existence of a small amount of Ce-carbonates is shown by the presence of a peak at about 1650 cm⁻¹, also present in the CeO₂ reference, although water may contribute to this region. This peak is particularly evident on all samples of the CZAm series. Despite this, the analysis of the whole IR spectrum shows the dominant presence of Ca-carbonates; these materials contain unidentate (bands at 1500, 1420, and 1060 cm⁻¹) and bidentate (bands at 1550, 1315, and 1050 cm⁻¹) species.^{41,42} The fact that these species are not detected by any diffraction technique (including electron diffraction) evidences the lack of long range order. As a general result, the analysis of the 1450–1300 cm⁻¹ region indicates the coexistence of unidentate and bidentate species for all series of samples. On the other hand, the microemulsion method seems to favor the presence of bidentate species with respect to the citrate method. This latter may be an inherent property of the preparation method but the different calcination temperatures (500 vs 600 °C) should also be considered to explain the result (although not big differences are expected as a function of the calcination temperatures mentioned above in view of the TG-MS data).

A quantitative estimation of the amount of Ca-carbonates was done by using TG-MS, and results from these experiments are summarized in Table 1. The measured amount of carbonate phase always grows with the Ca content in the materials and is lower for samples of the CZAc series. Assuming that such a phase was mainly of the CaCO₃ type, as the IR suggested,^{41,42} the (Ce + M)/Ca atomic ratio of the oxide phase was evaluated. Departures from the expected values of the Ca atomic content of the oxide materials are in the ±0.07 atom fraction interval. Table 1 also includes the values for Ca and O atom distributions into the oxide and carbonate phases. A point to stress is the fact that carbonate phases may play a role on the properties examined

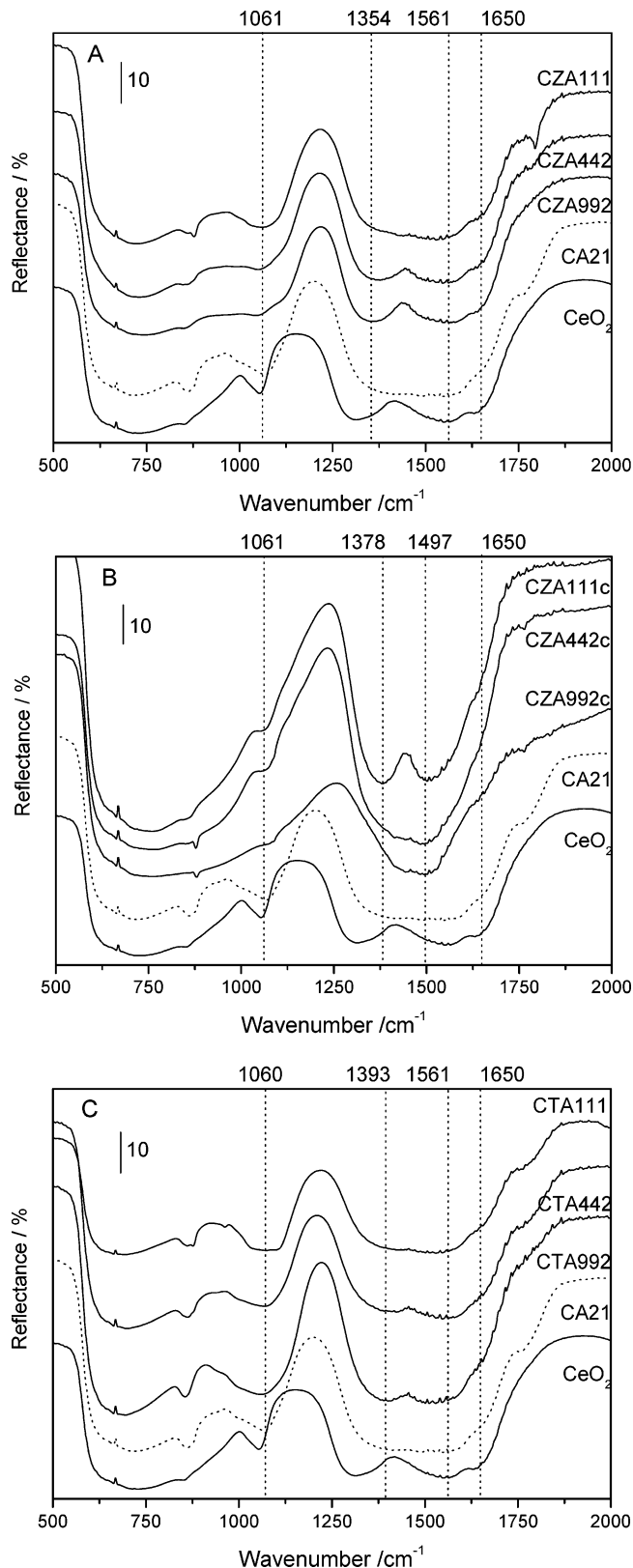


Figure 2. DRIFTS spectra of the Ce_{1-x-y}M_xCa_yO₂ (M = Zr, Tb) samples: (A) CZAm, (B) CZAc, and (C) CTAm series of samples. The notation used to label the mixed-metal oxides is explained in section II.1

in this work. As can be seen in Table 1, the Ca atomic distribution gives large values for the Ca present in the carbonate phase for all samples in the CZAm/CTAm series, while the O atom distribution indicates its major presence on oxide phases. Such data should be considered when interpreting absorption techniques (section III.3).

- (39) (a) Segall, M. D.; Pickard, C. J.; Shah, R.; Payne, M. C. *Phys. Rev. B* **1996**, *54*, 16317. (b) Sánchez-Portal, D.; Artacho, E.; Soler, J. M. *J. Phys.: Condens. Matter* **1996**, *8*, 3859.
- (40) Wiberg, K. B.; Rablen, P. R. *J. Comput. Chem.* **1993**, *14*, 1504 and references therein.
- (41) Fukuda, Y.; Tanabe, K. *Bull. Chem. Soc. Jpn.* **1973**, *46*, 1616.
- (42) Mikkelsen, A.; Engelsen, S. B.; Hansen, H. C. B.; Larsen, O.; Skibsted, L. H. *J. Cryst. Growth* **1997**, *177*, 125.

Table 1. Thermogravimetric Analysis of Ce–M–Ca Samples

	weight ^a (%)	(Ce + M)/Ca ^b content	Ca carb. ^c (atom %)	O carb. ^c (atom %)
CZA992	2.6	0.93:0.07	57	6
CZA442	4.5	0.85:0.15	42	10
CZA111	8.7	0.74:0.26	43	17
CZA992c	1.4	0.92:0.08	18	2
CZA442c	1.8	0.82:0.18	12	2
CZA111c	3.6	0.70:0.30	13	6
CTA992	3.8	0.96:0.04	63	9
CTA442	6.1	0.88:0.12	46	12
CTA111	6.6	0.73:0.27	27	14

^a Expressed as CaCO₃. ^b (Ce + M); Ca content of the oxide phase expressed as (Ce,M)₂Ca₃O₇. ^c Ca, O percentage present in the carbonate phase.

III.2. Structural Properties of Ternary Ce–M–Ca Solid Solutions. Figure 3 shows TR-XRD results obtained after heating the samples with a Ce/M/Ca atomic ratio of 1:1:1 in the three series studied. An analysis of the data at 25 °C (initial spectrum) points to the existence of nanosize diffracting entities which give rise to fluorite-type patterns indexed in the *Fm3m* space group for all cases. Table 2 summarizes the lattice constants and O occupancy factors for samples of the CZAm series from a Rietveld refinement of our XRD data taken at the X17B1 beam line ($\lambda = 0.1655$ Å). Table 2 also includes an estimation of the average particle size and strain from the width of the diffraction lines.^{5,32} In previous studies we have found that this approach yields particles sizes that agree with those determined by transmission electron microscopy.^{8,11b} The width of the diffraction lines effectively shows the nanosize nature of our samples. XRD data, on the other hand, give evidence of the somewhat larger particle size that can be obtained by using the citrate method: about 4.5 versus 3.0 nm for all samples of the CZAc versus CZAm series. This difference in primary particle size is roughly consistent with the BET area difference displayed by the samples calcined at 600 °C: 20–37 versus 34–56 m g⁻¹ for the CZAc versus CZAm samples. The BET areas calculated from the XRD-derived particle size ($S_{\text{BET}} = 6 \times \rho^{-1} \times \text{size}^{-1}$; $\rho = 4$ g cm⁻³) are, however, one order of magnitude bigger than those experimentally obtained, indicating the significant interwoven occurring among particles after calcination at 600 °C. This result will be explained by analyzing the thermal behavior of the materials (see section III.4).

Although single-phase XRD patterns are observed for all samples, it must be noted that the relatively large width of the peaks, inherent to the nanosize nature of the materials, disallows extracting definitive conclusions to whether a small amount of segregated phases could be present. The presence of carbonate phases in our materials would support this claim. However, the presence of additional phases in the calcined materials can be discarded on the basis of the TR-XRD experiments up to 925 °C (see below). Additionally, the small size of these systems limits the accuracy of XRD-based structural analysis, and the *a* parameters listed in Table 2 in some cases could represent an average value for pseudocubic phases with slight tetragonal or related distortions. The DF calculations for bulk CZA111 predict an average unit cell that is pseudocubic with a small tetragonal-like distortion ($a = 5.27$ Å, $b = 5.26$ Å, and $c = 5.30$ Å). Ca addition to

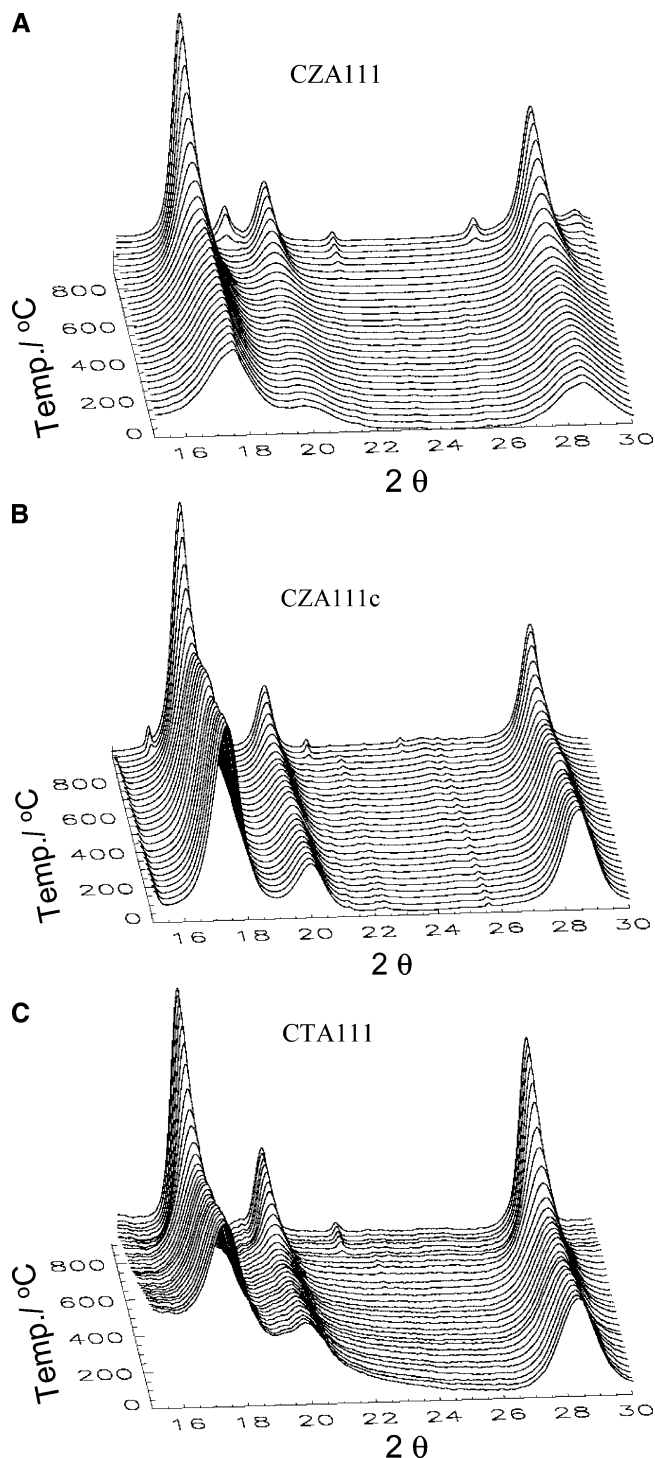


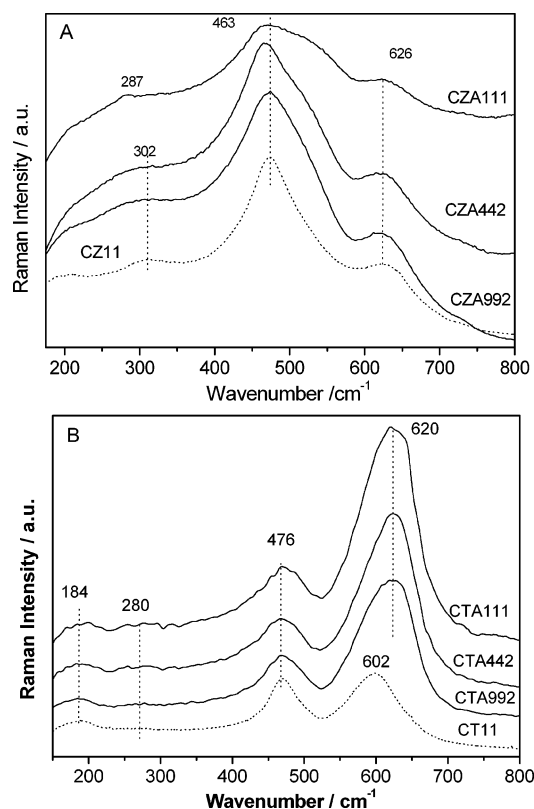
Figure 3. TR-XRD results obtained after heating of (A) CZA111, (B) CZA111c, and (C) CTA111 samples from 25 to 925 °C. Heating rate = 6 °C/min, and $\lambda = 0.922$ Å.

the Ce–Zr materials drives to small distortions of the *a* parameter for both preparation methods. The structural distortions from the fluorite-type structure can be analyzed by using RS.^{3,5,6,7,11,23,28,43} The CZA(m/c) RS spectra displayed in Figure 4A recall the corresponding one for the Ce/Zr (1:1) binary solid solution.^{8,11,23,24} No significant differences appear for the CZA materials although the citrate series seem better crystallized as judged by the better definition of the peaks (results not shown). Together with the F_{2g}-mode ceria-related peak at 460–475 cm⁻¹, Figure 4 shows the presence of additional peaks at about 620–630

Table 2. XRD Results for Ternary CZAm Solid Solutions and Reference Materials

sample	lattice constant, ^a <i>a</i> (Å)	O occupancy ^{b,c}	particle size ^a (nm)	strain ^a
CeO ₂	5.40	1.00	6.7	0.92
CZ11	5.28	0.99	5.0	1.75
CZA992 ^c	5.27	1.05 (1.02)	3.2	2.15
CZA442 ^c	5.26	0.92 (0.89)	3.0	2.41
CZA111 ^c	5.26	0.83 (0.78)	3.0	2.50
CA21	5.40	0.83	4.0	2.18

^a The estimated standard deviations are ± 0.01 Å for the lattice constants, ± 0.2 nm for the particle size, and ± 0.01 for the strain. ^b Without O vacancies, the value should be close to one. The derived sigma from least-squares analysis is ± 0.01 . Uncertainty arising from limitations in the model are of the order of ± 0.05 . ^c The first value corresponds to cation occupancies derived from actual Ca content (see Table 1), while values in parentheses correspond to cation occupancies for formal stoichiometry, assuming the exclusive formation of an oxide phase.

**Figure 4.** RS spectra taken at 300 K for a series of $\text{Ce}_{1-x-y}\text{M}_x\text{Ca}_y\text{O}_2$ ($\text{M} = \text{Zr}, \text{Tb}$) nanoparticles: (A) CZAm and (B) CTAm series.

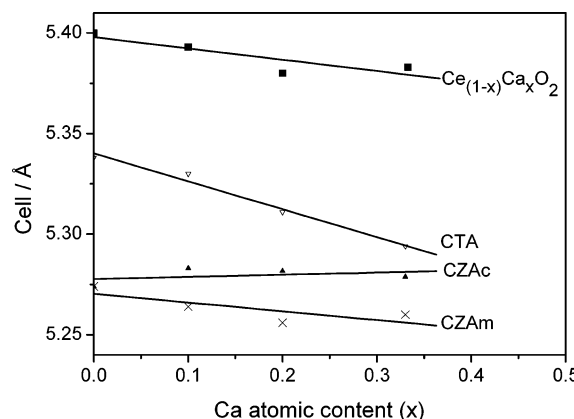
and $280\text{--}300\text{ cm}^{-1}$, and a shoulder around 550 cm^{-1} for the CZA(m/c) series. The mentioned bands are indicative of the existence of the so-called t'' tetragonal phase in all the materials studied while the 550 cm^{-1} shoulder is indicative for the presence of oxygen vacancies.^{5,6,7,23,43} This t'' phase is a pseudocubic phase with an a/c cell parameter ratio of 1. The RS result is, thus, in rough agreement with our DF calculations, which, as mentioned above, were able to confirm the tetragonal-like nature of the cell distortion.

Table 3 lists structural parameters for the CTA mixed-metal oxides determined from the Rietveld refinement of the XRD data taken at the X17B1 beam line ($\lambda = 0.1655$ Å). In Table 3, the addition of Tb and Ca to ceria induces a decrease in the cell parameter. The DF calculations for bulk CTA111, which showed a minor tetragonal-like distortion ($a = 5.29$ Å, $b = 5.30$ Å, and $c = 5.33$ Å), correctly predicted the

Table 3. XRD Results for Ternary CTAm Solid Solutions and Reference Materials

sample	lattice constant, ^a <i>a</i> (Å)	O occupancy ^b	particle size ^a (nm)	strain ^a
CeO ₂	5.40	1.00	6.7	0.92
CT11	5.34	0.88	5.5	1.36
CTA992	5.33	0.86	4.0	1.68
CTA442	5.31	0.83	5.3	2.05
CTA111	5.29	0.72 ₅	6.0	2.26
CA21	5.40	0.83	4.0	2.18

^a The estimated standard deviations are ± 0.01 Å for the lattice constant, ± 0.2 nm for the particle size, and ± 0.01 for the strain. ^b Without O vacancies, the value should be close to one. The derived sigma from least-squares analysis is ± 0.01 . Uncertainty arising from limitations in the model are of the order of ± 0.05 .

**Figure 5.** Lattice constants determined by XRD at 25 °C for nanoparticles of $\text{Ce}_{1-x}\text{Ca}_x\text{O}_2$ and $\text{Ce}_{1-x-y}\text{M}_x\text{Ca}_y\text{O}_2$ ($\text{M} = \text{Zr}, \text{Tb}$). The notation used to label the mixed-metal oxides is explained in section II.1.

larger cell volume shrinking detected with the simultaneous presence of Zr and Ca with respect to Tb and Ca. Again, the tetragonal-like distortion is consistent with the trends seen in Figure 4 for the RS spectra of the CTA samples. In the CTA series, differences with the binary Ce–Tb reference (known to be distorted from the ideal fluorite structure)^{11b} are mostly restricted to the energy position and intensity of the 620 cm^{-1} peak. As explained below, a major effect of Tb can be invoked to justify this phenomenon if the nature of this mode is somewhat localized,¹¹ but its invariance in the CTA ternary series may in fact indicate the existence of a compensation-like effect between structural effects induced by the lattice shrinking (see Table 3 and Figure 5) and a dominant influence of oxygen vacancies,⁴³ which may justify the net red shift with respect to the binary Ce–Tb reference (Figure 4).

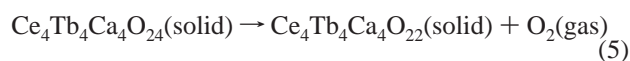
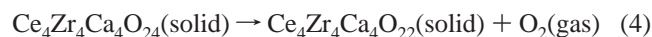
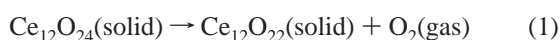
Figure 5 illustrates the cell parameter (a) behavior as a function of the Ca atomic content of the ternary materials and the corresponding binary Ce–Ca solid solution references.²⁸ A difference in the CZA series as a function of the preparation method is clearly visible, indicating, as discussed later, variations in the local order which influence the structural parameters measured by XRD as well as the Raman shape. The behavior of the ceria cell parameter in the presence of doped cations has been recently reviewed by Mogensen;⁴⁴ as mentioned, for a simple solid solution the

(43) Mcbridge, J. R.; Hass, K. C.; Pointdexter, B. D.; Weber, W. H. *J. Appl. Phys.* **1994**, *76*, 2435.

(44) Mogensen, M. Chapter 15 in ref 3.

lattice parameter follows Vegard's rule. Several empirical relationships have been published between the Vegard's slope and the ionic radius and formal oxidation state of the dopant ions.⁴⁴ For divalent cations, the slope of the Vegard's rule becomes close to zero when the atomic radius of the element is between 1.04 and 1.11 Å, depending on the theory used to estimate it. Ca^{2+} (0.99 Å) shows a rather close radius and, as has been shown previously, typically displays small Vegard's slope values for Ce–Ca binary solutions.^{5,27,28,44} This "ideal" case seems to roughly hold also for Ca addition to binary Ce–Zr solid solutions but not for Ce–Tb. The simultaneous presence of Tb and Ca in a Ce-based ternary Ce–Tb–Ca solid solution drives to a nonideal behavior which is likely related to differences, among our ternary Ce–Tb–Ca samples, in the relative amount of C^{4+} versus C^{3+} cations (where C here means Ce/Tb) and the corresponding, intrinsic oxygen vacancies.^{7,11,15,16,27,28,43,44} As mentioned, a correlation has been established between the lattice parameter and the ionic size of doped cations present in the fluorite-type structure, which leads to lattice expansion upon substitution of C^{4+} cations (corresponding ionic radii are 0.97/0.88 Å for $\text{Ce}^{4+}/\text{Tb}^{4+}$) by C^{3+} cations (1.14/1.04 Å for $\text{Ce}^{3+}/\text{Tb}^{3+}$).^{43,44} Note that differences in particle size may also contribute to the lattice parameter change or variation, but these are not expected to drive to significant distortion until very small size, below 2 nm.^{5,15,16} So, excluding this last point, the slope behavior depicted in Figure 5 for the Ce–Tb–Ca materials would indicate a growing quantity of C^{4+} cations as the Ca content increases in the series. If these C^{4+} cations are assumed to be Tb^{4+} species, considering that a fluorite lattice expansion of 3.75×10^{-2} Å per atomic fraction of Tb^{3+} would be expected,⁴³ under the assumption of the Vegard's rule, 77% is expected for the Ce–Tb (1:1) reference. These Tb^{4+} fractions are about 49, 97, and 100% for the CTA992, CTA442, and CTA111 samples. As will be shown by the XANES analysis, the assumption that Tb is the cation changing the oxidation state through the CTAM series is essentially correct, but the Tb^{4+} fraction estimation following the Vegard's rule is not correct, although the trend as the Ca content rises is qualitatively correct. In any case, the structural results suggest a larger stabilization of the C^{4+} (Tb^{4+}) oxidation state as the Ca content increases in the CTAM series. Our DF calculations for bulk CTA111 show substantial variations in the structural parameters of the metal cations with respect to the coordination expected in a perfect fluorite-type crystal. The existence of multiple Ce–O, Tb–O, and Ca–O bond distances is not consistent with the ideal structure assumed in the Vegard's approximation.

Starting with the unit cell shown in Figure 1, we calculated the ΔE associated with the following reactions



The results of the DF calculations indicate that the energy

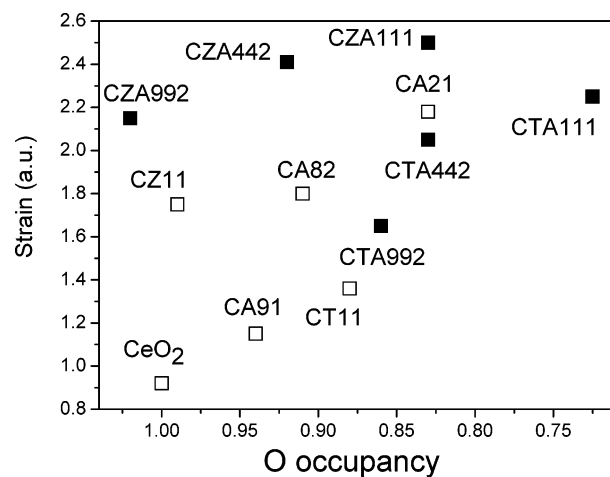


Figure 6. Strain versus O occupancy factors for materials of the CZAm and CTAM series (full symbols) and reference (open symbols) systems. The notation used to label the mixed-metal oxides is explained in section II.1.

necessary for the removal of O decreases following the sequence: $\text{Ce}_{12}\text{O}_{24} > \text{Ce}_6\text{Zr}_6\text{O}_{24} > \text{Ce}_6\text{Tb}_6\text{O}_{24} \approx \text{Ce}_4\text{Zr}_4\text{Ca}_4\text{O}_{24} > \text{Ce}_4\text{Tb}_4\text{Ca}_4\text{O}_{24}$. For pure ceria, reaction 1 is highly endothermic,^{3,5,28b} while for the ternary oxides reaction 4, $\Delta E = -0.38$ eV per cell, and reaction 5, $\Delta E = -0.46$ eV per cell, are exothermic. The inclusion of Ca into Ce–Zr and Ce–Tb favors the formation of O vacancies, a theoretical result that is in agreement with the trends inferred from the analysis of the XRD data (Tables 2 and 3).

The analysis of the oxygen vacancy distribution can be completed by using RS.^{5,15,16,43} In the case of the Ce–Zr–Ca samples, a loss of intensity is detected as the Ca content grows (Figure 4), which is more marked for samples prepared by using the microemulsion than the citrate preparation method. As this is not related to a color change or to significant changes in particle size (see Table 2), either an ordering effect in the oxygen vacancies so as to produce confinement of phonons within a nonhomogeneous distribution of domains and/or increasing structural distortions of the oxygen sublattice occurs as the Ca content grows. The asymmetry of the F_{2g} -mode peak with respect to the Ce–Zr reference (Figure 4A) is also pointing to the effect of the vacancy distribution on the Raman observables. Although the polydispersity of the size distribution may have an impact on Raman shape and intensity,^{5,15,16,43} the significant growth of the asymmetry and loss of intensity displayed on the CZA111 RS spectrum with respect to the remaining samples and binary Ce–Zr reference in fact indicate that an ordering effect is taking place as the Ca content of the materials is above 20 atom %. This conclusion is reinforced by the enhanced intensity of the second-order vacancy-related^{5,15,43} contribution at about 550 cm^{-1} (Figure 4). The influence of the Ca content on the vacancy distribution is further studied by analyzing the strain behavior of our materials. Figure 6 shows the strain behavior of our ternary Ce–M–Ca solid solutions prepared by microemulsion and reference materials. As the surface contribution to the strain is roughly constant (similar primary particle size) for each one of our sample series, the nanosized mixed-metal ceria-based solid solution strain differences among samples can be here primarily induced by a nonhomogeneous distribution of cations, the

creation of oxygen vacancies, and/or the presence of Frenkel-type vacancy-interstitial oxygen defects.^{5,7,45} Other punctual or extended defects (like dislocations, edges, cuts) can be also present.⁵ In the case of nanostructured ceria-based binary solid solutions, the main factor originating strain is related to the presence of oxygen-related vacancies.^{7,46} This is confirmed by Figure 6 which shows the growth of the strain with the decrease of the oxygen occupation parameter for all sample and reference systems. The presence of Zr as an alien species into the fluorite-type lattice is responsible for the large strain increment observed between the CZ11 and the CeO₂ references as well as the high value displayed by the CZA992 materials, despite its rather modest number of oxygen vacancies. In the CZAm series, the strain grows rather smoothly as the number oxygen vacancies increases but a nearly constant behavior is observed between CZA442 and CZA111 values. Again, this may point out to the existence of an ordering effect on the oxygen vacancy distribution for materials with a Ca content around 20 atom %, as above-mentioned on the basis of the RS. Because this behavior does not happen with the binary Ce–Ca reference system, we may suspect that local structural distortions, specific of the ternary solid solution, are in the origin of the ordering effect detected by the analysis of the RS spectra and the strain parameter. For the CZAc series the strain grows smoothly with the Ca content of the samples and displays a magnitude close to the value obtained for the CZ11 reference (1.68/1.80/2.21 vs 1.75 for, respectively, 992/442/111 vs CZ11), suggesting that the local order may not be affected so strongly by the Ca content of the Ce–Zr–Ca ternary system, if prepared by the citrate method. The comparison between the two preparation methods would indicate either a lower number of oxygen vacancies for the CZAc materials and/or, more likely, a different and less sensitive to Ca content local order for the CZAc series with respect to the CZAm one. A certain larger number of oxygen vacancies, which could be present in the CZAm samples, may be stabilized as a result of the lower particle size;⁵ this number should be, however, rather small if compared with that required to achieve charge neutrality in the presence of Ca²⁺. On the other hand, the likelihood of the point concerning differences in the local order homogeneity may be closely connected with the presence/absence of a germ for cationic ordering, as will be discussed in section III.4.

In the case of the Ce–Tb–Ca materials, the asymmetry of Raman peaks and particularly of the F_{2g} mode is less influenced by Ca content, at least with respect to the Ce–Zr–Ca series. In this case, the vacancy distribution is affected, as mentioned, by a growing quantity of C⁴⁺ cations as the Ca content increases; the easy C⁴⁺/C³⁺ redox behavior produces specific characteristics for the Ce–Tb–Ca materials as the Ca content of the material increases. Figure 6 displays the strain behavior for the CTA and reference materials. The CT11 reference gives a lower strain enhancement than CZ11 (having CeO₂ as a reference level) despite the lower number

Table 4. Calculated Mulliken Charges (e)

sample	<i>q</i> (Ce)	<i>q</i> (Zr)	<i>q</i> (Tb)	<i>q</i> (Ca)	<i>q</i> (O)
CeO ₂	1.42				−1.42
CaO				1.65	−1.65
CZ11	1.57	1.39			−1.48
CT11	1.48		1.47		−1.47
CZA111	1.49	1.34		1.86	−1.56
CTA111	1.46		1.49	1.88	−1.61

of oxygen vacancies of the latter; this would indicate that local distortions around Zr atoms and/or cation local order of the Fluorite-type lattice are of major relevance to justify this difference. The growing behavior of the strain with the oxygen occupancy decrease is also observed for the CZAm series, but here the presence of C⁴⁺ (Tb⁴⁺) allows the strain to be limited to low values with respect to the CZA(m/c) samples, even in the presence of a high number of oxygen vacancies, indicating a strong influence of the co-cation, for example, Tb, on the local order and vacancy distribution. The CTAm series behavior roughly resembles the binary Ce–Ca series one (similar slopes) but with a different ordinate zero (CT11 vs CeO₂); taking into account this and the Raman results, it can be suggested that no specific ordering effect seems to be triggered at a specific Ca content in the CTAm series.

III.3. Electronic Properties of Ternary Ce–M–Ca Solid Solutions. The electronic properties of the nanosize Ce–M–Ca solid solutions were investigated by using DF calculations and XANES. The results of the DF calculations for bulk CZA111 and CTA111 (see Table 4) indicate that the charges in the cations are far from the formal value of +4. Previous experimental and theoretical studies indicate that bulk CeO₂, Ce–Zr, Ce–Ca, and Ce–Tb are not fully ionic oxides^{5,8,11b} and are best described as ionocovalent compounds or covalent insulators.^{6c,8} The valence bands of the oxides contain not only O(2p) character but also a significant contribution from orbitals of Ce, Zr, and Tb. Table 4 compares Mulliken charges calculated for bulk CeO₂, CaO, CZ11, CT11, CZA111, and CTA111. In the ternary oxides, there is an important contraction of the cell parameters with respect to CeO₂ that leads to a reduction in the Ce–O bond distances and, thus, should give an increase in the positive charge of cerium. For the Ca atoms, the positive charge in CZA111 and CTA111 is larger than on CaO. This can be attributed to an increase in the number of oxygen neighbors for the Ca cations when going from the rock salt structure of CaO to a fluorite structure in the ternary oxides. Accordingly with cation charges, the oxygen negative charge increases in the ternary oxides with respect to CeO₂ and also with respect to the CZ11 and CT11 references.

XANES measurements were taken at all cation edges; as a general result, our cation edges do not show significant differences between the CZAm and CZAc series of samples. Concerning the common elements to all materials, the Ce L_{III} edge showed white line contributions at an energy position and with a shape close to those of the CeO₂ reference (Figure 7).^{47,48} A difference is, however, visible in the relative

(45) Mamontov, E.; Egami, T.; Brezny, R.; Kovanne, M.; Tyan, S. J. *J. Phys. Chem. B* **2000**, *104*, 11110.

(46) Martínez-Arias, A.; Fernández-García, M.; Hungria, A. B.; Conesa, J. C.; Munuera, G. *J. Phys. Chem. B* **2003**, *107*, 2667.

(47) (a) Fernández-García, M. *Catal. Rev.—Sci. Eng.* **2002**, *44*, 59. (b) Chen, J. G. *Surf. Sci. Rep.* **1997**, *30*, 1.

(48) Soldatov, A.; Ivanchenko, T. S.; Della Longa, S.; Kotani, A.; Iwamoto, Y.; Bianconi, A. *Phys. Rev. B* **1994**, *50*, 5074.

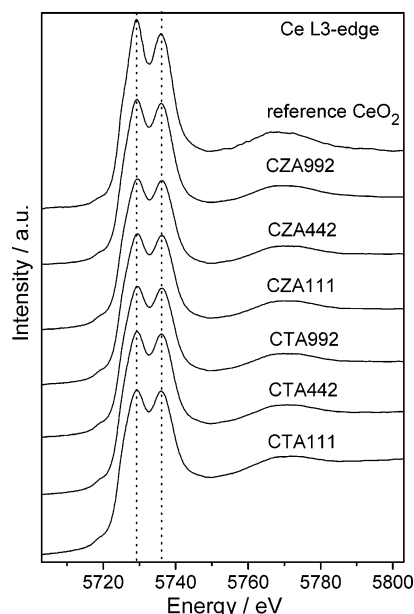


Figure 7. Ce L_{III}-edge XANES spectra for CeO₂ and Ce_{1-x-y}M_xCa_yO₂ (M = Zr, Tb) nanoparticles taken at room temperature.

intensity of the two peaks of the white line. The first peak, located at about 5729 eV and ascribable to a $[*]4f^{n-1}L^{n-1}5d^1$ final state, loses intensity with respect to the second one, which corresponds to a $[*]4f^0L^n5d^1$ final state. This can be, thus, related to a small modification of the Ce(4f/5d) energy level relative energies by interaction with the anions, reflecting a modest change of covalency on the Ce–O bond by the effect of the heterocations present in the fluorite structure. This effect is, however, small and appears to be insensitive to the nature of the heterocation, suggesting that it is mostly associated to changes in the local environment geometry and distances and/or related to small size differences. Apart from this, the Ce L_{III} edge showed the absence of significant quantities of Ce³⁺ which would lead to the appearance of a single contribution on the white line region peaking at about 5725 eV.^{47,48} This confirms that the C³⁺ cations described in section III.2 are not Ce³⁺.

Figure 8 displays the Ca K-edge XANES spectra for the CZAm and CTAm series of samples. As discussed in section III.1, the signal from the samples may contain a contribution from Ca carbonates, which may be of importance for all materials of the CZAm and CTAm series. In any case, Ca carbonates display distinctive features and a main continuum resonance at around 4048 eV;^{49b} the absence of such features indicates that our Ca K-edge XANES shapes are not significantly influenced by the presence of such phases. Moreover, while the Ca distribution seems dominated by carbonates in some samples, in others it is dominated by the oxides (Table 1), but all XANES shapes (Figure 8) are similar and must include a well-defined contribution from phases with long-range order (XRD visible), for example, oxide phases. The relatively low influence of carbonates on Ca K-edge XANES shape could be understood if the Ca–

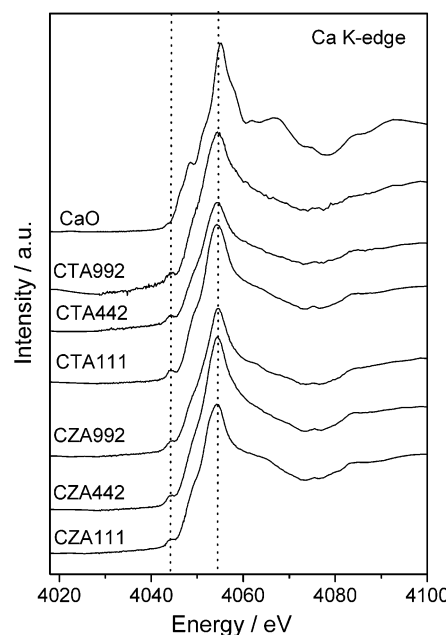


Figure 8. Ca K-edge XANES spectra for CaO and Ce_{1-x-y}M_xCa_yO₂ (M = Zr, Tb) nanoparticles taken at room temperature.

carbonates display a significant disorder at a local level, and, thus, their contribution to the XANES spectra would be mainly reflected in a broadening effect of the shape. This may be expected for a phase which exclusively exists at the surface of the material. On a first approximation, this broadening seems to be the main effect of Ca–carbonate presence on the XANES spectra depicted in Figure 8. The line shape for the Ca-containing ternary solid solutions shows differences with respect to pure CaO.⁴⁹ Differences with CaO reflects, in the first place, the geometrical local structure of the Ca cations into the oxide lattice. This produces the existence of a new pre-edge transition at about 4045 eV, the strong intensity change at around 4050 eV and, together with the inherent disorder nature of the materials, the practical disappearance of the RCs above 4060 eV. On the other hand, Ca K-edge XANES spectra display strong similarities among all of our ternary Ce–M–Ca solid solutions, pointing to a more or less constant local order (geometry and distances) around this cation. Apart from that, density-functional theory (DFT) calculations (Table 4) showed an increase of the Ca oxidation state when going from CaO to our ternary solid solutions, as was also detected for binary Ce–Ca solid solutions.²⁸ Electronic and structural (local) differences between Ca inclusion in Ce–Zr and Ce–Tb solid solutions seem small in view of Figure 8 and the DF results (Table 4). The higher Ca oxidation state would displace the Ca K edge to higher energies with respect to the CaO reference; however, the complex line shape of the pre-edge and edge regions, particularly influenced by the already mentioned broadening effect, precludes the extraction of a similar conclusion from an experimental point of view.

The Zr K-edge XANES spectra for a bulk ZrO₂ material and the nanosized Ce–Zr–Ca solid solutions prepared by the microemulsion method are displayed in Figure 9. At room temperature, a monoclinic crystal structure is the thermodynamically stable phase for microsize or bulk ZrO₂.^{5,6} The two main features in the Zr K edge correspond to electronic

(49) (a) Asokan, K.; Jan, J. C.; Chiou, J. W.; Pong, W. F.; Tsai, M.-H.; Shih, H. L.; Chen, H. Y.; Hsueh, H. C.; Chuang, C. C.; Chang, Y. K.; Chen, Y. Y.; Lin, I. N. *J. Phys.: Condens. Matter* **2001**, *13*, 11087. (b) Levi-Kalishman, Y.; Raz, S.; Weiner, S.; Addadi, L.; Sagi, I. *J. Chem. Soc., Dalton Trans.* **2000**, 3977.

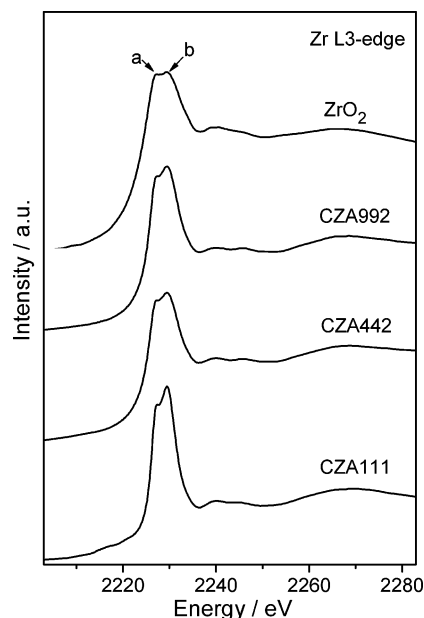


Figure 9. Zr K-edge XANES spectra for ZrO_2 reference and $\text{Ce}_{1-x-y}\text{Zr}_x\text{Ca}_y\text{O}_2$ nanoparticles taken at room temperature.

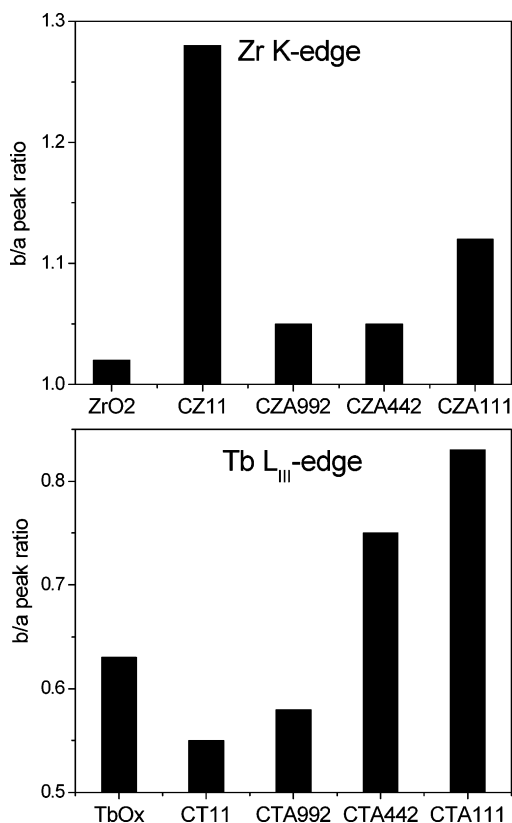


Figure 10. Intensity ratio for Zr K- and Tb L_{III}-edge white line resonances.

transitions from the occupied $\text{Zr}(2p)$ orbitals to the empty $\text{Zr}(4d)$ orbitals, which are split into t_{2g} and e_g symmetries.^{47,50} In oxides, the relative intensity of these two peaks strongly depends on the chemical environment properties (local symmetry, charge, and distances) around the Zr cations.^{8,47,50} Figure 10 displays the relative intensity (measured by the height) of these two peaks in the CZA samples and the binary Ce–Zr (1:1) reference. This picture gives evidence that Zr

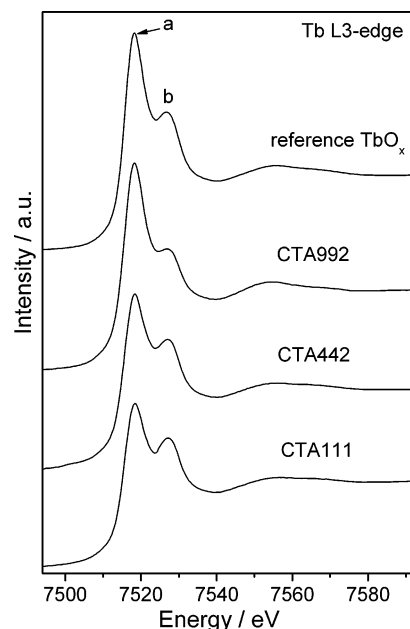


Figure 11. Tb L_{III}-edge XANES spectra for TbO_x reference and $\text{Ce}_{1-x-y}\text{Tb}_x\text{Ca}_y\text{O}_2$ nanoparticles taken at room temperature.

local coordination is progressively departing from a monoclinic, 4 + 3, first oxygen shell coordination to a more pseudocubic t'' one (4 + 2), characteristic of the CZ11 reference.^{6,8,31,51} Apart from the coordination number change on the Zr–O first shell, Figure 10 indicates a concomitant elongation of the average Zr–O bond distance with respect to the ZrO_2 reference, which, however, is, at maximum, for the CZA111 sample, midway to that corresponding to the binary Ce–Zr solid solution reference (ca. 0.04 Å).⁸ When Zr replaces Ce in the fluorite-type CeO_2 structure, the average Zr–O bond length becomes larger than that in the ZrO_2 reference and Ce loses charge density.⁸ For the ternary Ce–Zr–Ca solid solutions the presence of Ca moderates Zr-induced structural and electronic local changes around Zr cations. This is a proof of the existence of $\text{Ca}^{2+} \leftrightarrow \text{O}^{2-} \leftrightarrow \text{Zr}^{4+}$ interactions, which in this case, are of moderate magnitude.

Figure 11 illustrates the Tb L_{III}-edge XANES results obtained for ternary Ce–Tb–Ca solid solutions. Comparison with the TbO_x reference (probably Tb_4O_7 ,⁵² stoichiometric TbO_2 is very difficult to be prepared)¹³ indicates important differences in the white line region. As for Ce, Tb in the 4+ higher oxidation state shows two peaks in this region and the presence of a single peak at the low energy region of the white line if Tb^{3+} is present.^{11,13,47,48,52} In the case of Tb oxides, the high to low energy peak intensity ratio increases as the Tb^{4+} content does.^{11,13,52} This ratio, also included in Figure 10, grows in our ternary Ce–Tb–Ca samples with the Ca content, indicating the increasing presence of Tb^{4+} concomitantly to the increase of the Ca content of the material. It, thus, clearly showed that the presence of the voluminous Ca cation and the corresponding $\text{Ca}^{2+} \leftrightarrow \text{O}^{2-} \leftrightarrow \text{Tb}^{n+}$ interaction drives the Tb to the higher oxidation state, as was anticipated by the structural characterization. The

(50) Thomat, N.; Noguera, C.; Gautier, M.; Jollet, F.; Duraud, J. P. *Phys. Rev. B*, **1991**, *44*, 7904.

(51) Nagai, Y.; Yamamoto, T.; Tanaka, T.; Yoshida, S.; Nonaka, T.; Okamoto, T.; Suda, A.; Sugiyura, M. *Catal. Today* **2002**, *74*, 225.

(52) Karnatak, R. C. *J. Alloys Compd.* **1993**, *192*, 64.

quantity of Tb^{3+} is, however, reasonably larger when compared with those estimated from the XRD data, going from about 40 to about 20% as the Ca content grows in the CTAm series. As can be extracted from the CR intensity ratio displayed in Figure 10, these figures are typically larger than the corresponding Ce–Tb (1:1) reference system,¹¹ suggesting that Ca is able to stabilize Tb^{4+} , at least for samples having a Ca content above 10%. The dominant presence of Tb^{4+} is also evident in the DF calculations. After removing oxygen from bulk CTA111, the DF results show an insignificant reduction in the positive charge of the Tb cations. This is in clear contrast to the case of CT11 or CZT111, where the electrons left behind by the removal of oxygen occupy Tb(4f,5d) bands.²⁴ In this respect, the effects of the metal \leftrightarrow oxygen \leftrightarrow metal interactions in the CTA111 system are opposite to those seen previously for CZT111.²⁴ In the case of CZT111, $\text{Zr}^{4+} \leftrightarrow \text{O} \leftrightarrow \text{Tb}^{n+}$ interactions facilitate the generation of Tb^{3+} .²⁴ This and previous DF studies allow this to be associated with a short-range geometrical effect; it appears that Zr presence favors the preferential location of oxygen vacancies as first neighbors of Tb ions with respect to the Ca case.^{11,24} On the other hand, the presence of different Tb oxidation states as a function of the co-cation present into the fluorite-type structure may give an explanation to the increase of the net negative charge of oxygen atoms in the CTA111 systems with respect to CZA111 and CT11 (Table 4).

III.4. Sintering of $\text{Ce}_{1-x-y}\text{M}_x\text{Ca}_y\text{O}_2$ Nanoparticles. Figure 3 presents the TR-XRD data results for the three samples having a Ce/M/Ca atomic ratio of 1:1:1 while heating in dry air from 25 to 925 °C. These samples display the exclusive presence of fluorite-type diffracting entities at 25 °C, but when the temperature is increased above 750 °C, new diffraction peaks are typically detected in these three samples. These peaks are not observed for the samples having 9:9:2 and 4:4:2 Ce/M/Ca atomic ratios, indicating the stability of materials having Ca contents below about 20 atom % through the whole temperature ramp. The CMA111 (M = Z, T) samples should suffer some chemical/physical changes at high temperature. However, they seem of different nature in the three samples displayed in Figure 3. For the CZA111 sample, the four peaks detected have 2θ positions which could be associated with the presence of cationic order in the fluorite-type structure, in a similar way to that detected for the *kappa* phase of the CZ11 sample.⁵³ The short- to medium-range anionic ordering effect detected by RS and strain measurements on the calcined material may be likely linked with this high-temperature effect although the new XRD peaks cannot correlate with any expected from Ce-containing binary/ternary mixture defect ordered phases (Ce_6O_{11} , Ce_7O_{12} , Ce_2O_3 , and related phases). The peak appearing at about 22.1° could be alternatively associated with CaO .⁵⁴ The TP-XRD result for CZA111 means that presence of Ca favors cationic ordering with respect to the binary CZ11 reference.^{5,6,46,53} For the CZA111c material, we detected small peaks which, due to their sharpness and the

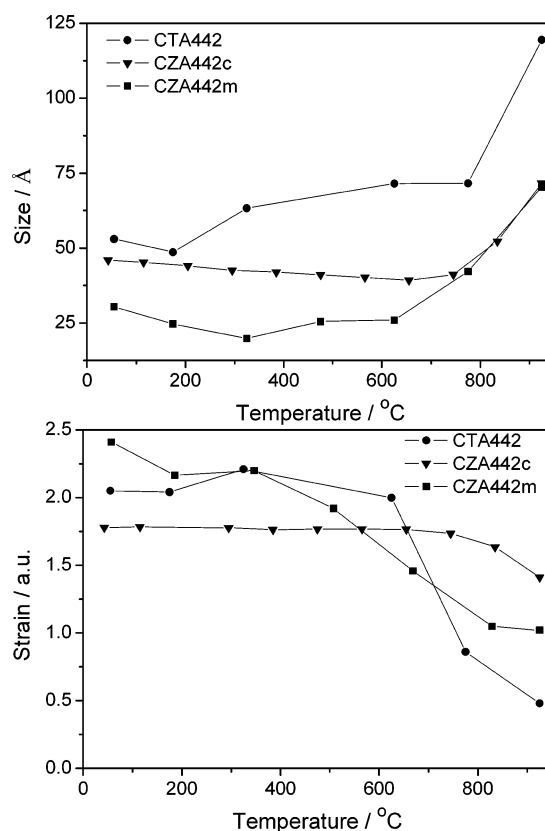


Figure 12. Effect of temperature on the particle size (top panel) and lattice strain (bottom panel) of the $\text{Ce}_{1-x-y}\text{M}_x\text{Ca}_y\text{O}_2$ (M = Zr, Tb) nanoparticles having a 4:4:2 Ce–M–Ca atomic ratio.

absence of concomitant, abrupt changes in the fluorite-type peak positions, could be ascribed to a Ca-containing phase. However, the known Ca oxide or carbonate phases would yield diffraction patterns not matching the present. The possibility of a temperature-induced ordering effect of the (anionic) defect distribution can be also mentioned, but as it occurred with the CZAm materials, there is no matching with known Ce_xO_y XRD profiles. Despite the absence of a clear assignment, it is evident that the presence of Zr increases the Ca solubility limit into the Fluorite structure with respect to the Ce–Ca solid solutions.²⁸ Fine details of the process seems to be dependent on the preparation method, but both the microemulsion and the citrate methods improve the behavior of the parent binary Ce–Ca solid solution. The CTA111 XRD result does show, on the other hand, the presence of CaO ⁵⁴ at high temperature, possibly indicating the extraction of a small fraction of Ca from the ternary solid solution. Nevertheless and according to the TG-MS results, the Ca source could be the carbonate phase instead of the oxide one.

Analysis of the TR-XRD data is presented in Figures 12 and 13. Figure 12 displays the particle size of the samples with a Ce/M/Ca atomic ratio of 4:4:2 as a function of the temperature. These results are representative of the three sample series behaviors, although the samples having 1:1:1 atomic ratios suffer from specific chemical/physical phenomena above 750 °C, as already described. Particle size does not vary significantly from the binary Ce–M parent samples^{8,11} and remains constant up to temperatures around 600 °C. The ternary solid solutions start to agglomerate once

(53) Izu, N.; Omata, T.; Otsuka-Yao-Matsuo, S. *J. Alloys Compd.* **1998**, 270, 107.

(54) Huang, Q. *Physica C* **1994**, 227, 1.

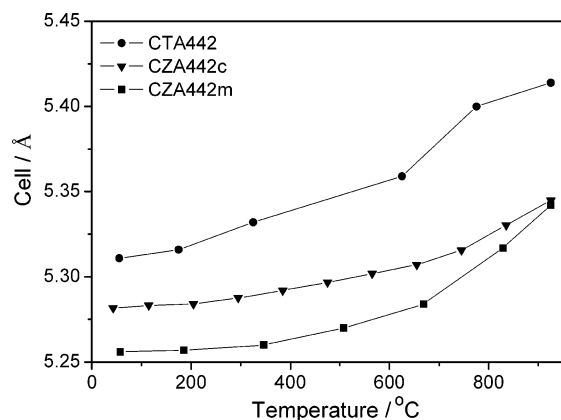


Figure 13. Cell dimension as a function of temperature for the $\text{Ce}_{1-x-y}\text{M}_x\text{Ca}_y\text{O}_2$ ($\text{M} = \text{Zr}, \text{Tb}$) nanoparticles having a 4:4:2 Ce–M–Ca atomic ratio.

the temperature is above 600 °C, although all samples of the CZAc series initiate this process a little late, around 700 °C. This difference is likely an effect of the different calcination temperature. The agglomeration rate measured from the slope of results displayed in Figure 12 appears to be more or less constant for each series (CZAm, CZAc, and CTAm) but increases in the order $\text{CZA} < \text{CTA} \ll \text{CeO}_2$. As mentioned, Zr and Tb ions improve the morphological stability of ceria nanoparticles, but Ca does not.^{8,11,28} In the case of ternary solid solutions, the combination of Zr and Ca seems to maintain the good thermal properties ascribed to the Zr presence but with the potential improvement of the oxygen handling properties derived from the presence of Ca;²⁸ this happens in the whole range of compositions studied here as the solubility limit seems significantly improved with respect to the Ce–Ca binary reference²⁸ for Ce–Zr–Ca materials prepared by both methods. In fact, the final size obtained for all CZAm/c samples after the thermal treatment is below 7.5 nm, a figure rather close to or even smaller than that corresponding to the binary Ce–Zr (1:1) reference.⁸ The combination of Tb and Ca again maintains a similar thermal behavior to that displayed by the binary Ce–Tb reference, yielding final sizes above 10 nm,¹¹ values a little bigger than those corresponding to the Zr–Ca combination.

At the bottom of Figure 12 one can see the presence of high levels of strain in our materials. The starting values are listed in Tables 2 and 3. As was discussed in section III.2, in our materials the main structural factor dominating strain behavior through our Ce–M–Ca series of samples is related to the presence of oxygen vacancies. Figure 12 indicates that when the system starts to agglomerate there is a concomitant release of strain. This is a typical behavior of nanosize materials and primarily corresponds to the decrease of the surface contribution to the strain as size increases.^{5,7} Additionally, Ce-based nanomaterials stabilize oxygen vacancies, which in turn are lost with the growth of size occurring during the thermal treatment.^{8,11,15,16,24,28} An interesting point is that the strain of the sintered materials, after the thermal treatment, in the Ce–Zr–Ca system seems to depend on the preparation method; independently of the Ca content of the sample, a larger strain remains in the citrate samples compared with the microemulsion one. As size does

Table 5. Values of the Thermal Expansion Coefficient (Å K^{-1})

sample	thermal expansion coefficient ($\times 10^5$)	sample	thermal expansion coefficient ($\times 10^5$)
CeO_2	6.34	CTA992	10.14
CZA992	6.22	CTA442	9.84
CZA442	6.10	CTA111	7.47
CZA111	5.62		

not appear as a differential factor between CZAm and CZAc series at high temperature (Figure 12, top), the strain behavior would be certainly related to differential local structural properties in turn related to the vacancy distribution, as already discussed. In fact, Cimino et al. indicate that minimizing $\text{M}_1\text{--O--M}_2$ heterocation bonds could be an effective mechanism to release strain in oxide solid solutions.⁵⁵

At room temperature the cell parameters of all Ce–M–Ca samples were displayed in Figure 5. As is well-known, inclusion of Zr and Tb decreases the cell parameter following Vegard's rule, although the $\text{Tb}^{4+}/\text{Tb}^{3+}$ ratio influences the slope.^{5,6,8,11,43,44} The addition of Ca to the CZ11 and CT11 samples varies the cell parameter as was described in section III.2. The thermal evolution of the cell parameter while heating in dry air from 25 to 925 °C is displayed in Figure 13 for samples having a Ce–M–Ca ratio of 4:4:2. The CMA442 samples exemplify the behavior of all samples on the corresponding CZA(m/c) and CTAm series. Two different regions with a linear behavior are typically detected in the cell parameter variation as a function of the temperature.^{8,11,24,28,44} These regions are separated by a breaking point between them, less defined for the CZAc series, at 600–700 °C. The initial region has a smaller slope and is dominated by the thermal expansion of the cell. An estimation of the thermal expansion coefficient is given in Table 5 and was measured during the cooling part of the ramp. The coefficient for nanostructured CeO_2 ($6.34 \times 10^{-5} \text{ Å K}^{-1}$) is consistent with previous work summarized in the review of Trovarelli.⁵⁶ Larger radius and lower charge than Ce^{4+} of cations present in the fluorite-type structure must increase the thermal expansion coefficient value and vice versa.⁴⁴ In our ternary solid solutions the combination of Zr^{4+} (smaller radius) and Ca^{2+} (larger radius; lower charge) produces smooth changes, although the trend observed as the Ca content grows in the CZA series is opposite to that expected on the exclusive basis of the Ca cation presence (see Table 5). This demonstrates that $\text{Ca}^{2+} \leftrightarrow \text{O}^{2-} \leftrightarrow \text{Zr}^{4+}$ interactions are playing a role on the thermal behavior of the CZA samples. Tb^{3+} presence has the effect of increasing the thermal expansion coefficient value,^{11,44} but in the presence of Ca the effect is strongly enhanced (see Table 5). Again, the effect of increasing Ca content on the CTA series behavior is opposite to the trend expected, but here the $\text{Tb}^{3+} \rightarrow \text{Tb}^{4+}$ “oxidation reaction” occurring in a parallel way to the Ca content growth is having a significant impact. After the region dominated by the thermal expansion of the cell, a second region of linear behavior is detected; the onset temperature is unequivocally associated with the starting point of the agglomeration process (compare Figures 12 and

(55) Cimino, A.; Stone, F. S. *Adv. Catal.* **2002**, 47, 141.

(56) Trovarelli, A. Chapter 2 in ref 3.

13) and, thus, describes a modification of the cell parameter as the particle size grows.^{5,8,11,23,24,44} As mentioned above, the starting point on the Ce–Zr–Ca materials depends on the preparation method, but rather close values are obtained by the end of the experiment. On the other hand, similar slopes are detected for the CZAm and CTAm series, indicating again the strong stability effect of Zr and Tb on the primary size of the materials.

IV. Summary and Conclusions

Synchrotron-based TR-XRD, XANES, RS, and IR spectroscopies and first-principles DF calculations were used to study the structural and electronic properties of Ce–M–Ca (M = Zr, Ca) oxide nanoparticles. All materials have a fluorite-type structure with the presence of oxygen vacancies to achieve charge neutrality.

Ce–Zr–Ca materials display the Fluorite-type structure with a tetragonal-like distortion and a cell parameter fairly independent of the Ca content. The local order of the ternary solid solution is, however, dependent on the Ca content; particularly, Zr ions vary their local coordination, losing oxygen neighbors and having growing Zr–O distances with the Ca content of the material. The preparation method seems to influence the primary particle size, smaller with the microemulsion method, and, more importantly, the cation/oxygen vacancy distribution(s), with the appearance of an ordering effect affecting the vacancy distribution (for Ca content near or above 20 atom %) in the case of the microemulsion preparation procedure. Ce–Zr–Ca electronic properties vary rather smoothly with Ca content, with main differences concerning the Zr(4d) splitting induced by the variation of its local symmetry. Ca addition to a CZ11 reference seems to yield structural and electronic properties not far from the mentioned reference, except by the mentioned local to medium order effects related to cation/oxygen vacancy distributions.

Ce–Tb–Ca materials also display the fluorite-type structure with a tetragonal-like distortion but having a cell parameter which decreases with the Ca content. The simultaneous presence of Tb and Ca into the fluorite-type lattice distorts local order, for example, metal–oxygen distances, as judged by the DF results. The cell parameter behavior through the Ce–Tb–Ca series is associated mainly to a $\text{Tb}^{3+} \rightarrow \text{Tb}^{4+}$ “oxidation process” occurring in parallel to the Ca content growth on the ternary solid solution. Stabilization

of Tb^{4+} appears as a natural way to reduce the strain (and energy) of the fluorite lattice of the samples and could be related to the progressive disfavor of the presence of anion vacancies as first neighbors of Tb cations. This Tb oxidation process seems to minimally perturb the co-cations Ce and Ca electronic states. Structural and electronic properties of the Ce–Tb–Ca materials are, thus, dominated by $\text{M}^{n+} \leftrightarrow \text{O}^{2-} \leftrightarrow \text{Tb}^{m+}$ ($\text{M}^{n+} = \text{Ca}^{2+}, \text{Ce}^{4+}$) interactions which are not present in the corresponding parent binary Ce–Tb solid solutions.

The structural and electronic properties of the solids determine their thermal behavior. In the case of Ce–Zr–Ca materials, it is shown that both preparation methods allow increasing the solubility limit of Ca into the fluorite-type structure with respect to the parent Ce–Ca solid solution. The microemulsion method, however, seems to favor the development of some kind of an ordering effect (intimately related with both cation and vacancy distributions) at high temperature with respect to the citrate method and also to the binary Ce–Zr reference systems, yielding solid solutions essentially stable below 925 °C. At the end of the thermal treatment, both preparation procedures only differ in such a structural (e.g., ordering) property, giving materials with a similar, small primary particle size and similar cell parameters. In the case of Ce–Tb–Ca materials, a small CaO segregation would occur but high thermal stability of the primary particle size is also observed with respect to the parent binary Ce–Tb reference system. The ternary Ce–M–Ca solid solutions seem, thus, good candidates for the potential uses described in the introduction section, as they maintain the thermal stability of Ce–Zr and Ce–Tb systems but increase the solubility limit of Ca into the fluorite-type structure, with the potential enhancement of the chemical reactivity associated with the presence of oxygen vacancies.

Acknowledgment. The research carried out at the Chemistry Department of Brookhaven National Laboratory was financed through Contract No. DE-AC02-98CH10886 with the U.S. Department of Energy (Division of Chemical Sciences). The NSLS is supported by the Divisions of Materials and Chemical Sciences of DOE. Work at the “Instituto de Catálisis y Petroleoquímica (CSIC)” was done with financial support from CICYT (Project No. CT2004-03409/BQU). Thanks are given to Dr. M. Bañares for the use of the Raman spectrometer and Dr. Z. Zhong for his help at beamline X17B1.

CM050265I